



# Assessment of deep cryogenic heat-treatment impact on the microstructure and surface chemistry of austenitic stainless steel

Patricia Jovičević-Klug<sup>a,b,\*</sup>, Nataša Lipovšek<sup>a</sup>, Matic Jovičević-Klug<sup>c</sup>, Maruša Mrak<sup>b,d</sup>, Jernej Ekar<sup>b,e</sup>, Bojan Ambrožič<sup>f</sup>, Goran Dražić<sup>b,g</sup>, Janez Kovač<sup>b,e</sup>, Bojan Podgornik<sup>a,b</sup>

<sup>a</sup> Institute of Metals and Technology (IMT), Lepi pot 11, Ljubljana 1000, Slovenia

<sup>b</sup> Jožef Stefan International Postgraduate School, Jamova cesta 39, Ljubljana 1000, Slovenia

<sup>c</sup> Max Planck Institute for Iron Research, Max-Planck-Straße 1, Düsseldorf 40237, Germany

<sup>d</sup> Slovenian National Building and Civil Engineering Institute, Dimičeva ulica 12, Ljubljana 1000, Slovenia

<sup>e</sup> Department of Surface Engineering, Jožef Stefan Institute, Jamova cesta 39, Ljubljana 1000, Slovenia

<sup>f</sup> Centre of Excellence in Nanoscience and Nanotechnology, Jamova cesta 39, Ljubljana 1000, Slovenia

<sup>g</sup> Department of Materials Chemistry, National Institute of Chemistry, Hajdrihova ulica 19, Ljubljana 1000, Slovenia

## ARTICLE INFO

### Keywords:

Deep cryogenic treatment

XRD

HRTEM

SEM

XPS

ToF-SIMS

## ABSTRACT

This systematic study deals with the influence of deep cryogenic treatment (DCT) on microstructure and surface properties of austenitic stainless steel AISI 304 L on different length scales and in the surface region. The study incorporates different analysis techniques, such as light microscopy, scanning electron microscopy (SEM), energy dispersive X-ray spectroscopy (EDS), electron backscatter diffraction (EBSD), high-resolution transmission electron microscopy (HRTEM), X-ray photoelectron spectroscopy (XPS) and time-of-flight secondary ions mass spectrometry (ToF-SIMS). DCT modifies the microstructure of treated samples through promoted precipitation of Cr<sub>7</sub>C<sub>3</sub> carbides, induced twinning and  $\alpha$ -martensite formation. Additionally, XPS/AR-XPS and ToF-SIMS results also provide evidence of modified oxidation dynamics of DCT samples compared to conventionally heat-treated samples with increase of the Fe-oxide fraction and lower Cr-oxide fraction in the surface oxide layer. An evaluation of oxidation states and ions distribution within the surface layer of deep cryogenically heat-treated stainless steel AISI 304 L is conducted with XPS/ToF-SIMS. These results are correlated with the microstructural changes and nitrogen diffusivity induced by DCT, which are associated with modified oxidation behaviour of AISI 304 L. These results provide further understanding of DCT dynamic on the overall microstructure and the corresponding surface behaviour.

## 1. Introduction

Stainless steels are widely used in everyday lives and are important structural and protective materials in high corrosive and oxidative environments from nuclear powerplants and nuclear storage [1], marine pipelines as part of offshore plants [2], aerospace [3], marine industry [3], implants [4], robotics [5], automotive industry [6], mining [7], pharmaceutical and chemical industry [3,8] to food industry [8]. Stainless steels are remarkable due to their unique combination of corrosion and oxidation resistance and mechanical properties, as well as due to their versatility formed by their different microstructures induced through processing, heat treatment and alloying [9]. Mechanical properties of stainless steels are strongly linked to their chemical composition

(Cr, Ni, Cu etc.) [10] and microstructure (austenite/martensite/duplex) [11]. However, corrosion and oxidative properties are strongly coupled with the formation of the initial oxide layer on the surface, which acts as a passivation film. The formation of the oxides in this layer is strongly connected to the oxidation kinetics, which determines the nucleation of specific type of oxide(s) [12]. This nano-scaled passive film is usually enriched with Cr, Mo, Ni-based oxides in the inner part (low Gibbs free energy), whereas the outer part is formed from Fe-enriched oxides [3,10,13]. In the last few years, the heterogenous distribution of Cr within passive film and its influence on local breakdown of passive film has been greatly discussed [13]. As such, the corrosion and oxidative resistance properties of stainless steels are of question and provoking new research to provide enhancements of their anti-corrosive and

\* Corresponding author at: Institute of Metals and Technology, Lepi pot 11, Ljubljana 1000, Slovenia.

E-mail address: [patricia.jovickevicklug@imt.si](mailto:patricia.jovickevicklug@imt.si) (P. Jovičević-Klug).

antioxidative properties. That is why studies, especially those focused on nuclear powerplants and nuclear waste storage [1], natural resources (oil, gas and coal) [14] and medicine [15], are now focusing on improving the corrosion and oxidative resistance of different stainless steels in order to prolong material life cycle to avoid primarily natural catastrophes (gas, oil and nuclear leakage) and to prevent biomedical emergencies (implant rejections, degradation and induced toxicity). To counteract the shortcomings in corrosion properties and ability to resist progressing chemical degradation of the surface (oxidation), the stainless steels are sometimes combined together with other materials in form of cases, coatings and composites: (1) polymers, such as thermoplastic polyurethane [16], (2) cement or bentonite [1] and (3) ceramic coatings [17]. Additionally, to such solutions, the additional option is to improve properties of stainless steels through their handling, such as heat treatment with novel processes or procedures. One of these is deep cryogenic treatment (DCT), which has arisen as a proven method to improve corrosion and oxidative resistance of different steels [18–24]. DCT is special by exposing the material to very low sub-zero temperatures (below  $-160^{\circ}\text{C}$ ) for certain time (usually 1 day) in order to alter materials' microstructure and to improve different materials' properties (corrosion and wear resistance, mechanical properties and fatigue resistance) [18,25–27]. Moreover, detailed literature survey showed that there is a scarcity of studies conducted on stainless steels in combination with DCT [28–33]. Furthermore, the only study, which has tested DCT treated stainless steels for corrosion resistance was conducted by Baldissera and Delprete [30], reporting observed no difference on corrosion resistance of the selected AISI 302 stainless steel. Therefore, the research in this field is more than needed in order to expand the potential of DCT in stainless steels on improving their corrosion resistance and conduct research in correlation to oxidative resistance. Additionally, further research is needed to also understand the microstructural and surface dynamics induced by DCT on stainless steels, in order to evaluate its practical feasibility in various industries and applications.

In the present work, the selected austenitic stainless steel AISI 304 L is used, as one of the most versatile stainless steels, to investigate how DCT influences the microstructure, surface chemistry and their development. The microstructural changes are investigated by light (LM), scanning electron (SEM) and high-resolution transmission electron (HRTEM) microscopy, whereas the phase changes are identified by X-ray diffraction (XRD). To observe changes induced on the surface of AISI 304 L and with-it development of initial oxidation/passivation layer (composition of oxide layer, thickness and stratification), surface sensitive techniques X-ray photoelectron spectroscopy (XPS) including angle resolved XPS (ARXPS) and time-of-flight secondary ion mass spectrometry (ToF-SIMS) are utilized. This study also acts as the fundamental research, or the next step, for the future research of DCT influence on corrosion resistance of AISI 304 L stainless steel.

## 2. Material and methods

### 2.1. Material and heat treatment

Selected material for testing was austenitic stainless steel AISI 304L, Frankstahl, Guntramsdorf, Austria. Steel was supplied in form of hot rolled annealed and peeled bars. Chemical composition of the alloy, measured by inductively coupled plasma optical emissions spectrometry (ICP-OES), Agilent 720, Santa Clara, CA, USA., is in wt. % as follows: 0.02 C, 1.71 Mn, 0.03 S, 18.22 Cr, 8.23 Ni, 0.48 Cu, 0.30 Mo and 71.01 Fe. For further analyses, the material was cut into samples of  $10 \times 10 \times 3$  mm size. Samples were treated with two types of heat treatments – conventional heat treatment (CHT) (groups C1 and C2) and deep cryogenic heat treatment (DCT) (groups DCT1 and DCT2). In addition to this, the groups were also tested at different solution-annealing temperatures in order to observe effect of DCT based on heat treatment parameters. Samples were heat treated and quenched in a horizontal vacuum furnace

Ipsen VTTC324-R, Kleve, Germany. Afterwards, the DCT samples were gradually immersed in  $\text{LN}_2$  for 1 day with cooling/warming rate around  $10^{\circ}\text{C}/\text{min}$ . The immersion was performed directly after quenching. The processing parameters of each sample is provided in Table 1. To compare the effect of the different heat treatment in relation to the prior microstructure, a group marked “as delivered” was used as a reference to observe changes induced by both heat treatments (CHT-groups C1 and C2 and DCT-groups DCT1 and DCT2). The group “as delivered” is without solution-annealing (state in which the material was delivered from the supplier).

### 2.2. Methods

For the analysis of the material from chemical, structural and microstructural point of view and to penetrate different portions of the surface and volume of the material, several techniques were employed (see Fig. 1).

#### 2.2.1. Microstructure characterization

The microstructure of individual samples was firstly investigated by light optical microscope (LM) Zeiss Axio Vario, Carl Zeiss, Oberkochen, Germany, with which the austenite grain size was measured according to standard ASTM E112-13. On selected samples the size and shape of the austenite grains were evaluated on 6 randomly chosen locations encompassing at least 50 grains for the analysis within 1 image field with size of  $85,863.71 \mu\text{m}^2$ . To reveal the microstructure, the sample was etched with Aqua regia mixture. The imaging was performed with Nikon Microphot, Tokyo, Japan. The image analysis was performed with program Stream Motion and mode Gran Intersect (Supplementary material 1 a). With the standardized measurements, the G (the class of grains) was obtained, which indicates the average grain size ( $\mu\text{m}$ ). The detailed statistics of austenite grains was performed with PASWStatistics18, IBM, Armonk, NY, USA and Origin 2021, OriginLab, Northampton, MA, USA.

In the next step, the samples were investigated by scanning electron microscope (SEM), energy-dispersive X-ray spectroscopy (EDX) and electron backscatter diffraction (EBSD) by using ZEISS Crossbeam 550 FIB-SEM Gemini II, Germany. SEM-EBSD mapping was achieved under vacuum conditions below  $10^{-6}$  mbar, acceleration voltage of 15 kV and current of 5 nA. The size of the scanned areas was  $100 \times 100 \mu\text{m}^2$  and step size  $0.4 \mu\text{m}$ . The interpretation of the EBSD results was performed using OIM Software, AMETEK, Mahwah, NJ, USA.

#### 2.2.2. TEM and STEM analysis

Samples (lamellas) for (scanning) transmission electron microscopy (S)TEM were prepared using FEI Helios Nanolab 650, FEI, Hillsboro, OR, USA, focused ion beam (FIB) at the Center of Excellence in Nanoscience and Nanotechnology – Nanocenter (CENN Nanocenter). During the sample preparation samples were protected with 300 nm thick electron deposited Pt layer and an additional  $2.5 \mu\text{m}$  thick ion deposited Pt layer, which were deposited on top of each other at the selected ion acceleration voltages/beam currents of: 20 kV/1.6 nA and 30 kV/0.4 nA, respectively. Final polishing of lamella was performed with FIB at 1 kV/100 pA for 1 min on each side, enabling the removal of the amorphous residue and gallium artifacts.

For nano-scale microstructure investigations, probe Cs corrected Scanning Transmission Electron Microscope (STEM), Jeol ARM 200 CF, Jeol, Tokyo, Japan, equipped with a high-brightness Cold Field Emission

**Table 1**  
Processing parameters for each investigated sample group.

Parameters	C1	DCT1	C2	DCT2
Solution-annealing	1080°C, 30 min		1000°C, 30 min	
Quenching procedure	with $\text{N}_2$ at 5 bars, $6.2^{\circ}\text{C}/\text{s}$ , $t_{800-500^{\circ}\text{C}} = 48$ s			
Cryogenic treatment	none	$-196^{\circ}\text{C}$ , 1 day	none	$-196^{\circ}\text{C}$ , 1 day

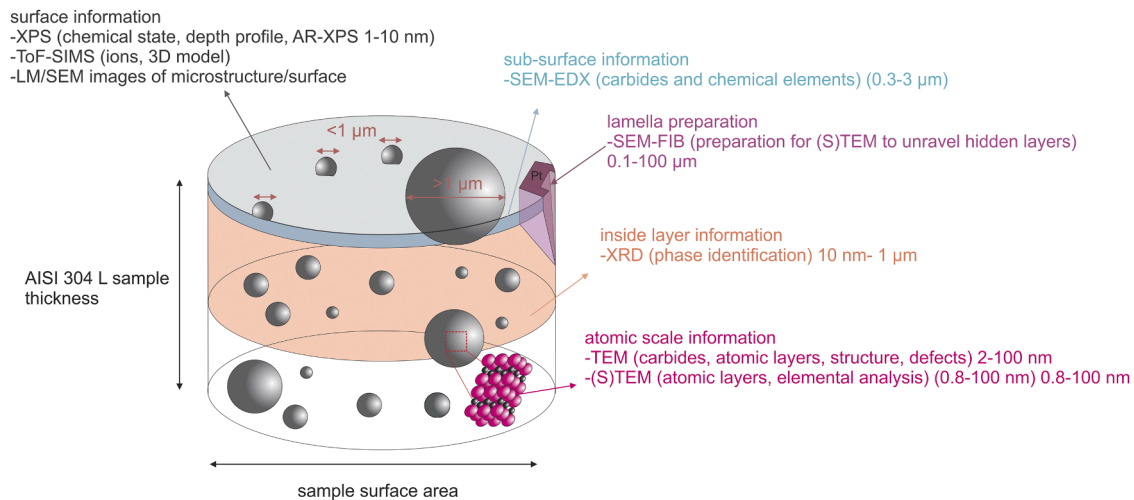


**Fig. 1.** The schematic representation of information obtained by different surface and bulk techniques (chemistry and microstructure/phase identification) in this study.

Gun (CFEG) operating at 200 kV was used. Qualitative and quantitative elemental chemical analyses were performed with Energy Dispersive X-ray spectroscopy using Jeol Centurio wide-area Silicon Drift Detector (SDD) system.

### 2.2.3. Phase analysis

Phase characterization was performed by X-ray powder diffraction using PANalytical Empyrean X-ray diffractometer (XRD), Malvern, UK, equipped with CuK $\alpha$  radiation with  $\lambda = 1.54 \text{ \AA}$ . The samples were scanned at 45 kV and a current of 40 mA, over the  $2\theta$  range from  $15^\circ$  to  $90^\circ$ , at a step size of  $0.013^\circ$  and time per step time 400 s. The phase identification was achieved using COD database references and their fractions were evaluated using a combination of Rietveld refinement [34] and Toraya method [35].

### 2.2.4. Surface characterization

**XPS analysis.** X-ray photoelectron spectroscopy (XPS) was performed by electron spectrometer PHI-TFA XPS, Physical Electronics, Chanhassen, MN, USA, with Al K-alpha as X-ray monochromatic source with the emission energy of 1486 eV. The explored area was 0.4 mm in diameter and analysis depth was between 3 and 5 nm. XPS spectra were measured in the energy range 0–1200 eV with the energy resolution of about 1.2 eV to identify and quantify the presence of different elements. XPS spectra with high-energy resolution (0.65 eV) were then recorded on two different surface locations of the samples to identify the chemical state of the elements present in the samples. This way the peaks of C 1s, O 1s, Cr 2p, Fe 2p and Ni 2p $_{3/2}$  were measured. Additionally, XPS depth profiles of chemical composition in the subsurface region were recorded on the samples C2 and DCT2 from surface to depth of about 10 nm. The samples were bombarded with Ar ions with energy of 3 keV over range of  $3 \times 3 \text{ mm}$ . The velocity of ion etching rate was about 1 nm/min. Additionally, the angle-resolved XPS was applied to probe different depth information at samples surface. The angle  $20^\circ$  was chosen to get more information of the oxide layer, so surface layer, whereas angle  $70^\circ$  was chosen to get spectral information related to the bulk of the samples. In addition, linear least squares (LLS) method was implemented on the XPS profile data to identify different chemical states of one element in the oxide/metallic surface interphase for elements C, Cr and Fe.

**ToF-SIMS.** The ToF-SIMS analyses were performed using a TOF SIMS 5 instrument, IONTOF, Münster, Germany. Depth profiles were recorded using two ion guns in a dual-beam depth profiling mode. Bi $^{+}$  primary ions of energy of 30 keV from a BiMn Liquid Metal Ion Gun was used as

the analysis beam. Their current was 1.0 pA. The analysed (information) depth was about 2 nm and the mass resolution  $m/\Delta m$  between 3000 and 9000, depending on the peak of interest. Secondary ions emitted from surface were analysed over the  $m/z$  range from 10 to 314. Cs $^{+}$  sputter ion beam with an energy of 500 eV was used for the depth profiling. The ion current of the Cs $^{+}$  ions was about 45 nA (velocity of 0.04 nm/s). The analyses with the Bi $^{+}$  primary ions were performed over a  $100 \times 100 \mu\text{m}$  scanning area ( $128 \times 128$  pixels), located in the centre of the  $400 \times 400 \mu\text{m}$  etching crater sputtered by the Cs $^{+}$  ion beam. H $_2$  flooding was applied during depth profiling to reduce matrix effect [36]. Hydrogen gas was introduced into the analysis chamber via capillary to a close proximity of the analysed region. The pressure of the H $_2$  atmosphere in the analysis chamber was  $7 \times 10^{-7}$  mbar.

## 3. Results and discussion

### 3.1. Austenite grains analysis

Fig. 2 represents the micrographs obtained by LM and SEM in order to determine the impact of DCT on the austenite grain (AG) size. The investigated stainless steel AISI 304 L displays overall a fairly homogeneous microstructure consisting of large austenite grains with twins. The etched microstructures also display voids, which are related to preferential etching of the material at inclusions and defects. Additionally, individual austenite grains hold martensite bands, which are associated with localized deformation and destabilization of the austenite [37]. However, the DCT samples seem to preferentially display more martensite compared to their control counterparts (more in the next sections).

The average G values for samples are 9 (as delivered), 8 (C1), 7.5 (DCT1), 8 (C2) and 7.5 (DCT2). The class values indicate on average a 5 % increase of AG size with DCT for both sample groups, which is supported by descriptive statistics of the measurements, provided in .. The G values indicate that with the additional heat treatment the AG grow, which later further expand with the application of DCT (Fig. 3a). A possible explanation of this phenomenon can be related to the relaxation of internal stresses through either phase transformations and/or dislocation annihilation [38]. The analysis of the twinning occurrence shows that DCT increased twinning formation by 5–10 %, which can introduce a higher fraction of mismatch zones and with it increased AG size (more in next section). Additional observations showed that groups C2 and DCT2 have a slight inhomogeneous size distribution of grains in relation to the core and edge regions (Fig. 3b), whereas the other two sample groups (C1 and DCT1) showed no significant spatial variation of the AG size.



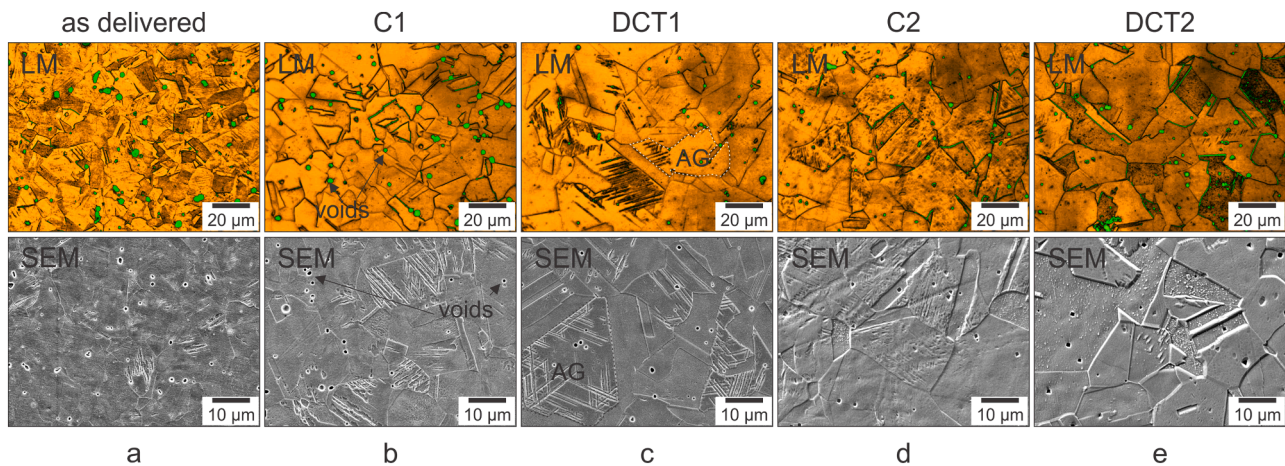


**Fig. 2.** Light microscopy (LM) and scanning electron microscopy (SEM) micrographs for each sample group with marked voids and austenite grains (AG); a-as delivered, b, d-control groups with conventional heat treatment C1 and C2; c, e-tested groups with deep cryogenic treatment DCT1 and DCT.

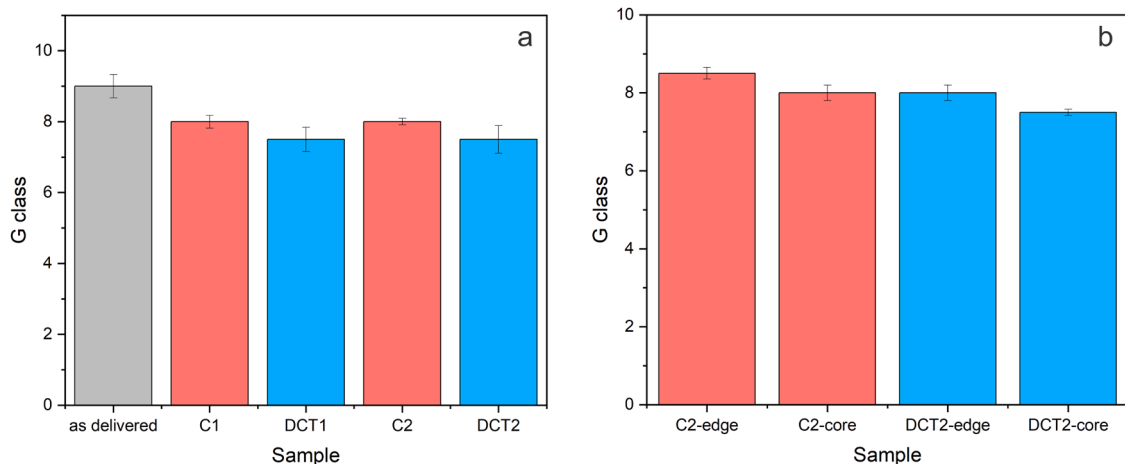


**Fig. 3.** The average class of grains (G value) for (a) different sample groups and (b) edge and core locations of PAG in samples C2 and DCT2.

Detailed statistical analysis confirmed the variation.

The ANOVA ( $p < 0.05$ ) showed statistically significant difference between the mean values of C2 and DCT2. Whereas post-hoc test Tukey HSD showed that there is no significant difference between C1 and DCT1 ( $p > 0.05$ ) and significant difference between groups C2 and DCT2 ( $p < 0.05$ ). Furthermore, the paired t-test between groups C2-edge/DCT2-edge and C2-core/DCT2-core showed for both cases insignificant difference ( $p > 0.05$ ), confirming the similar inhomogeneity related to the heat treatment and not to the application of DCT.

### 3.2. Detailed phase and microstructural analysis

The XRD results (Fig. 4) confirmed that the austenite (FCC) is the main phase for all samples, with a fairly similar amount of 85–86 wt. % for all samples. The samples display small amounts of  $\alpha$ -martensite (BCT), at which DCT2 has a much higher amount (1.9 wt. %) compared to the others (0.6–0.7 wt. %). However, all samples displayed comparable presence of  $\epsilon$ -martensite (HCP) of roughly 5–6 wt. % and  $\delta$ -ferrite of about 1.3 wt. %. The samples C2 and DCT2 indicate slightly higher amount of  $\epsilon$ -martensite compared to C1 and DCT1, which can be a result of the lower solution-annealing temperature.

The strongest difference between the samples is related to the carbide precipitation (see Table 2). The comparison of all samples shows clearly the effect of the higher solution-annealing temperature that leads to higher total carbide amount for C1 and DCT1 samples compared to

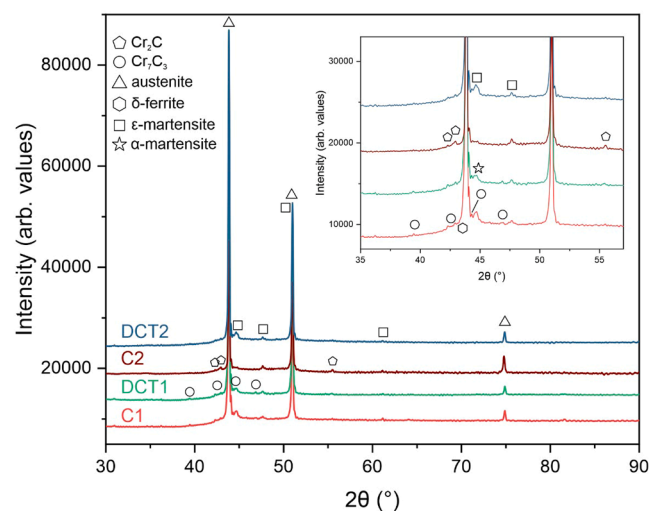


**Fig. 4.** X-ray diffraction (XRD) spectra for all investigated sample groups of AISI 304 L with enlargement depicting the individual peaks of interest and their identifications.



**Table 2**

Extracted fractions of individual phases from XRD data for each investigated sample of AISI 304 L.

AISI 304 L	C1	DCT1	C2	DCT2
Matrix (wt. %)				
Austenite	84.9	85.0	86.4	85.2
$\alpha$ -martensite	0.7	0.6	0.6	1.9
$\epsilon$ -martensite	5.1	5.2	5.7	5.9
$\delta$ -ferrite	1.3	1.2	1.3	1.1
Carbides (wt. %)				
M(Cr/Fe) <sub>7</sub> C <sub>3</sub>	6.0	5.8	2.8	4.0
Cr <sub>2</sub> C	2.0	2.2	3.2	2.1

the C2 and DCT2 samples. Additionally, the C1 and DCT1 samples displayed generally higher amount of M<sub>7</sub>C<sub>3</sub> carbides compared to C2 and DCT2. Furthermore, C1 and DCT1 displayed similar carbide fractions of both M<sub>7</sub>C<sub>3</sub> and Cr<sub>2</sub>C indicating no influence of DCT on carbide precipitation with higher solution-annealing temperature.

In contrast, C2 and DCT2 display a significant change in carbide fraction. The DCT2 sample displays higher amount of M<sub>7</sub>C<sub>3</sub>-type carbides (by 43 %) at the expense of smaller amount of Cr<sub>2</sub>C-type carbides, which are present in about 50 % higher amount in C2. From this perspective, the C2 sample is different from the other 3 samples in its significantly higher amount of Cr<sub>2</sub>C carbides, which is considered to be related to the solution-annealing temperature that dissolves preferentially the M<sub>7</sub>C<sub>3</sub> carbides, but with it allows reprecipitation into Cr<sub>2</sub>C carbides. Since the annealing temperature for C2 and DCT2 is lower than for C1 and DCT1, the amount of prior dissolved carbides is lower, leading to a lower saturation of the matrix with carbon. In turn, this leads to a change in precipitation type that prefers the precipitation and/or growth into Cr<sub>2</sub>C at the expense of Cr<sub>7</sub>C<sub>3</sub> carbides. With DCT, possibly the transition of the Cr<sub>2</sub>C carbides back to Cr<sub>7</sub>C<sub>3</sub> carbides is activated through the prior reformation of austenite into  $\alpha$ -martensite that allows subsequent carbide precipitation after DCT. As such, the Cr<sub>2</sub>C values fall to the similar values of the undissolved state that is determined from the samples C1 and DCT1 (approx. 2 wt. %).

EBSD mapping (Fig. 5) confirms the results extracted from the XRD. The emergence of  $\alpha$ -martensite (designated as BCC in the mapping) is highest for DCT2 sample, which are present in the form of irregular patches distributed randomly across the sample. In contrast, the other samples display similarly negligible presence of  $\alpha$ -martensite. The EBSD data indicates that DCT does not induce any preferential orientation of the austenite grains and twins. Nevertheless, the EBSD data indicates a higher segmentation of the microstructure of DCT1 and DCT2 compared

to the control counterparts that is associated to the higher twinning formation with DCT. High-magnification SEM images and EBSD maps confirm the presence of carbides that are formed both on the AG boundaries and within the grains themselves for all samples (Fig. 6). The carbides on the high-angle grain boundaries exhibit larger size and a high density of them along the twin grain boundaries. The carbides within the austenite grains form in a considerably high density, smaller average size and seem to form with an orientation dependency with the matrix. The latter can be seen from the preferential etching effect on the matrix under specific grain orientations that leave behind a spread of non-etched points that correspond to nano-carbides (see Fig. 6a, b, e and f). Local EDS probing confirmed an increased Cr (25 at. % and 34 at. %, matrix has approx. 18 at. %) and C (18 at. % and 12 at. %) content around the non-etched points related to the individual M<sub>7</sub>C<sub>3</sub> and M<sub>2</sub>C carbides. Additionally, EBSD indicates that both M<sub>2</sub>C and M<sub>7</sub>C<sub>3</sub> carbides form within the AG, which display different orientation dependency with respect to the AG (Fig. 6c, d, g and h). The M<sub>7</sub>C<sub>3</sub> carbides are crystallographically oriented differently from the matrix, whereas the M<sub>2</sub>C carbides follow the crystallographic orientation of the AG. In terms of preferential orientation of the carbides with respect to the austenite matrix, no differences could be determined between the investigated samples. Furthermore, no carbides type M<sub>23</sub>C<sub>6</sub> was detected by XRD/SEM/EBSD in any of the investigated samples.

As stated in previous section, one of the main newly obtained observations was that DCT additionally induced the formation of twins and nano-twins and thus the change of AG class. DCT minimizes tensile residual stresses, however, this is achieved by the simultaneous introduction of compressive stress with DCT due to shrinkage pressure effects [39]. From this, it is proposed that for austenitic steels, the additional compressive stresses lead to nanoscale destabilization of the lattice close to grain boundaries and defects, which causes the additional formation of twins and nano-twins in groups DCT1 and DCT2 (Fig. 7a–d). This also translates to formation of generally thinner twins within the AG, but also in higher density, when DCT is applied (see also Fig. 6). Similar observation of twin formation after DCT was observed by Gu et al. [40] and Che et al. [41], for non-ferrous alloys.

Further, high-resolution imaging reveals that individual grains can present high density of twins as seen in Fig. 7a. The twins seem to form preferentially around the regions that hold  $\epsilon$ -martensite and form in strides near the borders between austenite and  $\epsilon$ -martensite, further confirming the association of twins to local stressed/strained zones. Surprisingly, around  $\alpha$ -martensite patches nano-twins were found to extend radially from the patches. The radial form is considered to occur due to the lattice mismatch between  $\alpha$ -martensite and austenite that

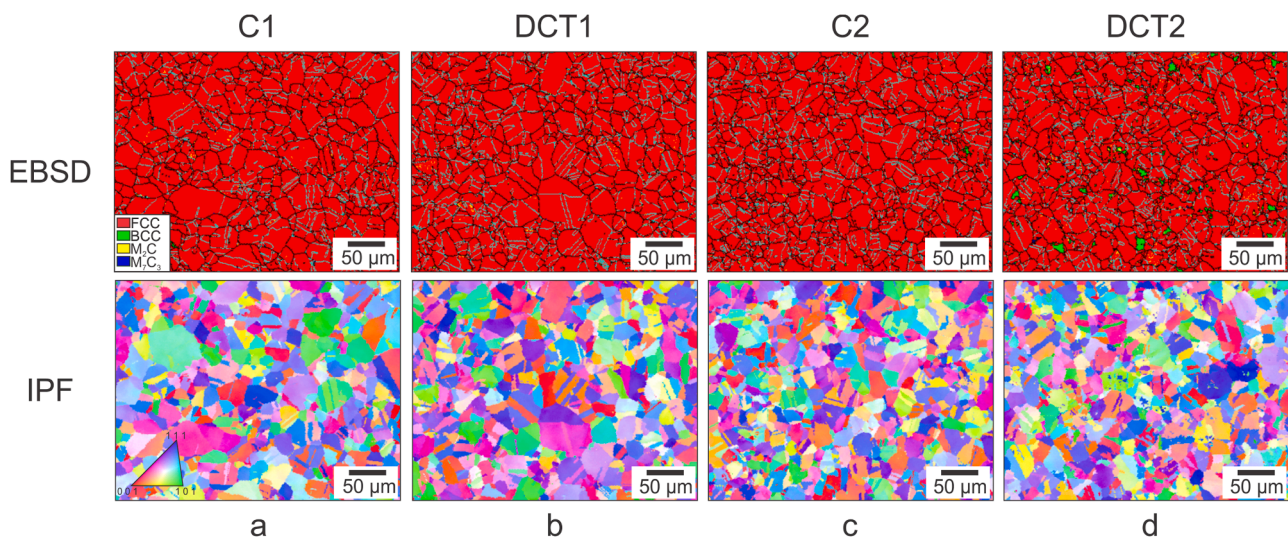


**Fig. 5.** EBSD and inverse pole figures (IPF) images of individual investigated samples, (a) C1, (b) DCT1, (c) C2 and d) DCT2.

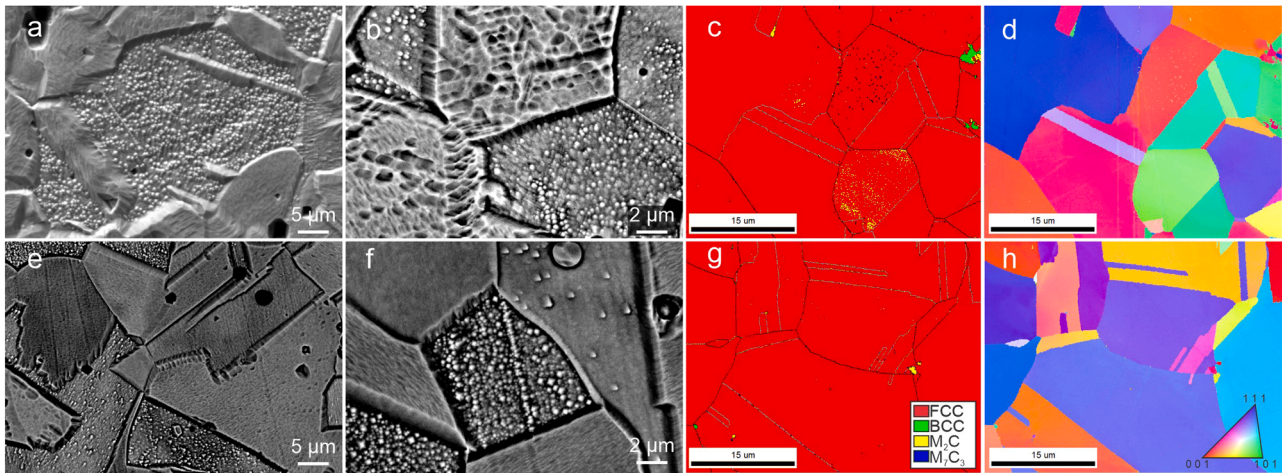


**Fig. 6.** Exemplar SEM images of (a, b) DCT samples (DCT1 and DCT2) and (e, f) control samples (C1 and C2) with EBSD phase and corresponding inverse pole figures (IPF) images for DCT (c, d) and control (g, h) samples.

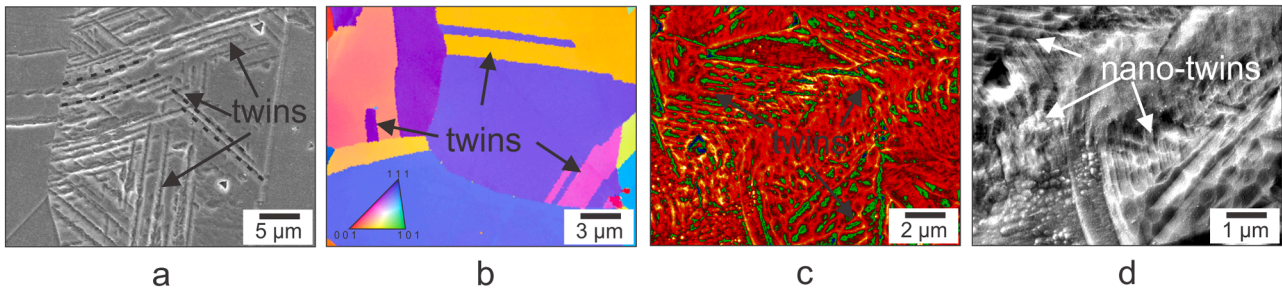


**Fig. 7.** Exemplar of twins (a) SEM image of formed twins, (b) inverse pole figures (IPF) image of twinned regions, (c) Color-coded image depicting the occurrence of nano-twins in regions holding ε-martensite, (d) High-magnification SEM image indicating the nano-twins formed around α-martensite regions.

induces additional strain-induced twinning from the interface. Due to the higher occurrence of α-martensite in sample DCT2, the nano-twinning around these patches was most obvious for sample DCT2, which also held the largest density of nano-twins from all the samples. The co-existence of both stress- and strain-induced transformations related to twinning phenomenon for AISI 304 has been also reported by other researchers [42].

### 3.3. TEM analysis

TEM investigation of the samples confirms the presence of both α-martensite and ε-martensite, which was observed for both control (Fig. 8) and DCT (Fig. 9) samples. Local SAED analysis confirms a tightly bound structure of regions of α-martensite that surround austenite twins (example in Fig. 8b for control samples and Fig. 9d for DCT samples). Additionally, the surrounding regions of these structures is followed by strands of ε-martensite (see SAED 1 from Fig. 8b) that form due to the local strain-induced transformation of austenite [39]. Near to the twinned austenite structures, carbides were also determined to be present in the form of M<sub>2</sub>C and transient structure that is considered to be related to the local carbon-rich zones formed with the formation of α-martensite [43]. The interesting feature of the control samples is the considerably high dislocation density (Fig. 8c and d) compared to the DCT samples (Fig. 9b–d). This furthermore supports the stress-state modification with DCT, as has been proposed and confirmed for other metallic materials [40,41]. Additionally, individual twinning faults are found to be scattered across all samples (Figs. 8c and 9c), confirming the presence of nano-twins within the material. Within the control samples the density of twin faults is lower compared to the twin fault density in DCT samples. Furthermore, the twin faults seem to form in a more

organized fashion in the case of control samples along specific directions/line (Fig. 8c and d), whereas in DCT samples the twin faults are sporadically formed and also show different orientation (seen by the orientation of the elongated feature of the twin faults in Fig. 9c). The twin faults are confirmed not to be carbides or similar through local EDS chemical mapping that confirm the equivalent chemical composition of the twins and twin faults (see .).

The higher twin fault density and random orientations are considered to be related to the dislocation density modification with DCT. It is believed that the dislocations agglomerate during the cryogenic cooling of the material that leads to the formation of nano-twins, which also explains the increased fraction of α-martensite caused by modification of the stress state of the material with DCT. This phenomenon also explains the modified carbide fraction determined from XRD, which can be understood by the formation of carbon-rich zones at the interfaces between twins and austenite/α-martensite regions. The presence of carbon-rich zones is associated to the additional peaks arranged in a hexagonal manner with large atomic distances of 2.55 nm and 2.44 nm for control and DCT samples, respectively. The peaks could not be correlated as any specific known carbide, matrix or impurity phase, making it more likely to be related to the displacement of interstitial atoms of the matrix phase in a specific low-symmetry quasi-structure. Nevertheless, the individual peaks could be partially related to a highly displaced M<sub>7</sub>C<sub>3</sub> carbide form due to the overlap with the individual peaks, however, since additional peaks to confirm such structure are missing in the obtained SAED, this could not be confirmed with certainty. Irrespectively of this, the TEM investigation proves the presence of nanotwins that are accompanied by regions of α-martensite that are promoted by the DCT. As such this provides a clear understanding for the initiation of further carbide development through the formation of additional grain boundaries and



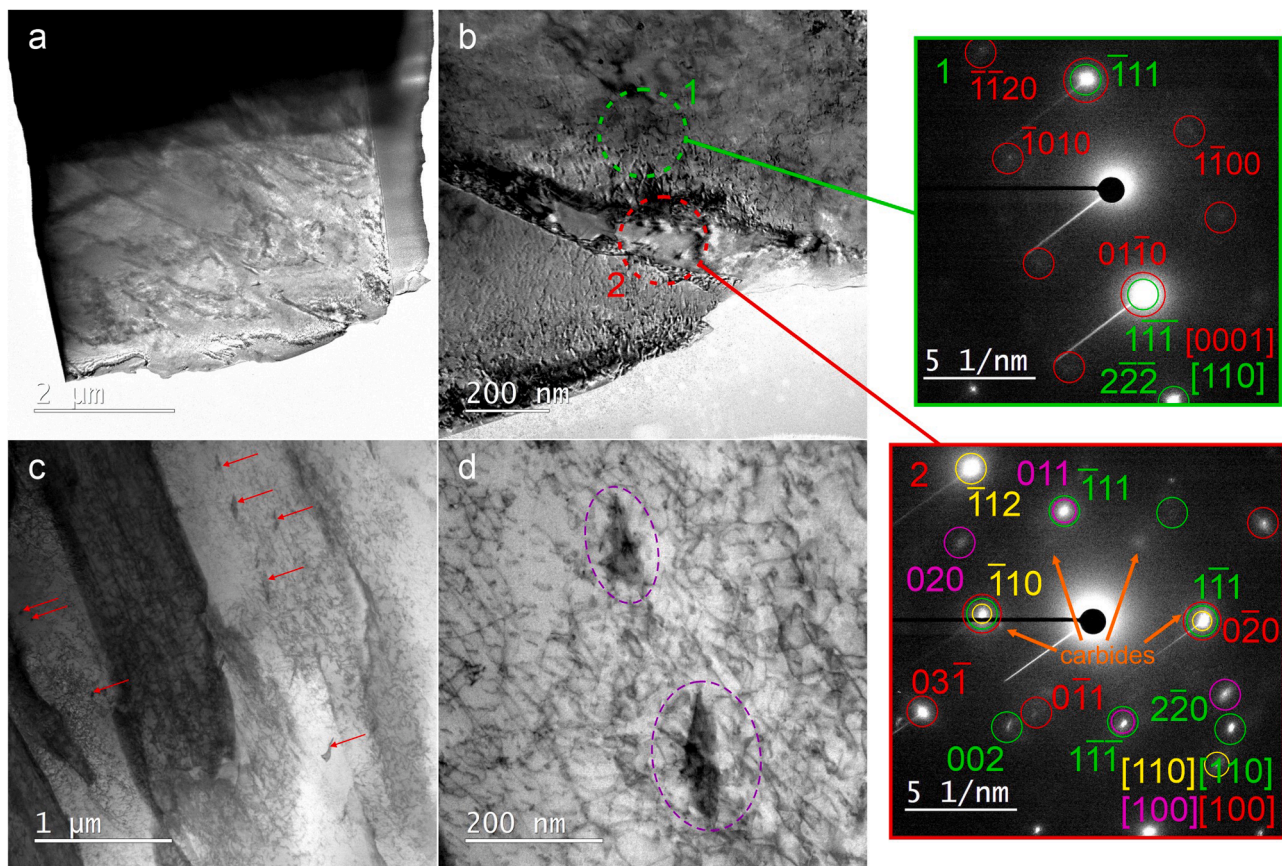


**Fig. 8.** (a) TEM image of investigated FIB lamella of C2 sample. (b) Selected region investigated with SAED. The SAED 1 displays austenite matrix (green colour) and  $\epsilon$ -martensite (red colour). The SAED 2 indicates that in the region of twinned austenite (green colour),  $\alpha$ -martensite is formed on each side, corresponding to two differently oriented  $\alpha$ -martensite structures (yellow colour and purple colour). Additionally, carbides are found in the form of  $\text{Cr}_7\text{C}_3$  (red colour) and transient structure (orange arrows) that corresponds to an arrangement of weak diffraction peaks with 0.255 nm spacing. (c) TEM image depicting twinned austenite structures with high dislocation density. The red arrows indicate the presence of twinning faults, which are enlarged and marked with purple dashed circle in (d).

interfaces that can hold larger amount of carbon [44]. In this respect, the transitioning to different carbide forms with DCT is also probably related to the carbon redistribution at the grain boundaries that leads to the distortion of the  $\text{Cr}_7\text{C}_3$  carbides towards the form of  $\text{Cr}_7\text{C}_3$  (from hexagonal to orthorhombic structure).

### 3.4. XPS and AR-XPS

Due to the higher difference in  $\alpha$ -martensite formation and stronger difference in carbide formation, samples C2 and DCT2 were selected for further investigation with XPS technique. XPS depth profile (Fig. 10) indicates a relatively similar oxide formation for both C2 and DCT2 samples in terms of their thicknesses. Taking into account sputtering rate of 1 nm/min we evaluated from XPS depth profiles the thickness of the surface oxide layer to be 1.5 nm and 1.3 nm for C2 and DCT2, respectively. However, a slight variation in the O 1s signal indicates higher presence of oxides on C2 sample surface compared to DCT2 sample surface (also see Supplementary material 3 of the step-by-step depth profile). The variation of the additional Cr 2p and Fe 2p signals suggests that the build-up of the oxides is different between the two samples, at which C2 displays a higher amount of Cr-based oxides compared to the DCT2 sample. The signals of all traced elements after 1 s of sputtering time ( $\sim 2$  nm) indicates that the samples are similar in terms of their bulk composition. The variation of oxygen can thus be explained by the higher fraction of  $\text{Fe}_2\text{O}_3$ , which correlatively modify the total atomic fraction of oxygen. To truly test this hypothesis, LLS analyses was performed on the XPS depth profiles to identify different chemical states of Fe, Cr and C as a function of depth. The LLS confirms

that the structure of the oxide layer is different between the two samples, despite the comparable overall oxide thickness for both samples (1.5 nm and 1.3 nm for C2 and DCT2, respectively). C2 sample displays a higher fraction of Cr and proportionally a lower Fe fraction in the oxide layer compared to DCT2 (compare Fig. 11b-e). The DCT2 sample also displays a deeper Fe-oxide component compared to the C2 sample (Fig. 11c), which is indicated by the persisting Fe surface signal after longer sputtering times (Fig. 11f). With the LLS analysis of the C1s signal (Fig. 11a and d), which show that analysed surface for C2 contains larger volume of carbides compared to the DCT2 sample surface. DCT2 in-fact shows negligible C1s signal after 0.5 s sputtering, indicating that no carbides were present in the investigated region of the material. With this, it is clear that the stronger Fe surface signal cannot be related to carbide formations and that it must occur due to the formation of different oxide subsurface and bounded state of Fe in the transiting oxide layer.

The two types of chemical states of Cr and Fe in the oxide structure and its variation between the two investigated samples is further confirmed with AR-XPS. With the analysis of probing more the surface (Fig. 12) and bulk (Fig. 13) portions of the samples (approximately 1 nm versus 3 nm), a clear trend can be determined. The surface-bound AR-XPS confirms a relatively comparable formation of the top-most portion of the oxides for both samples, covered by a carbon-based organic layer. In retrospect, the bulk-sensitive AR-XPS spectra confirm the differences between the samples as derived from the depth profiles. C2 sample displays a stronger Cr (III) oxide peak that confirms the higher oxygenation of the surface of the sample with Cr-based oxide compared to DCT2.

In contrast, the deconvolution of Fe indicates that DCT2 displays a



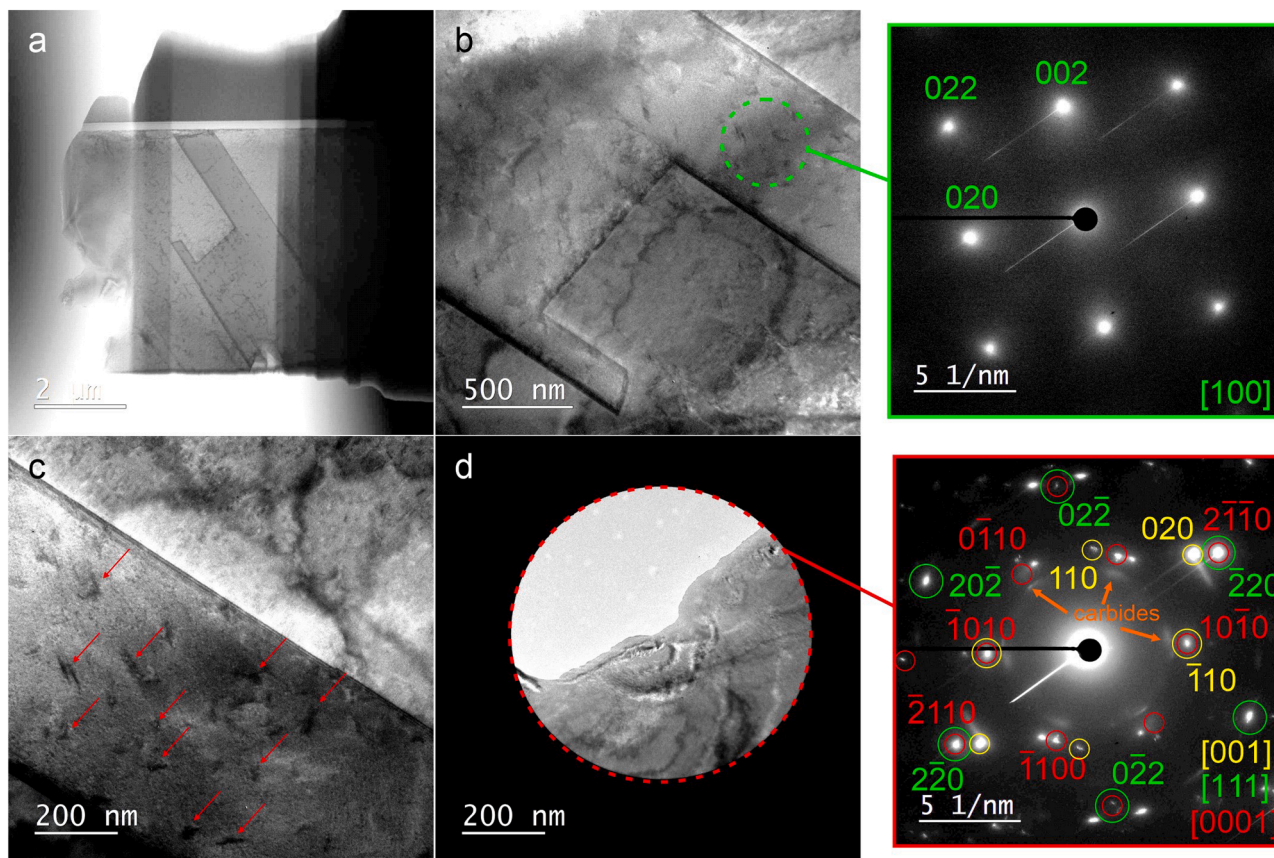


**Fig. 9.** (a) TEM image of investigated FIB lamella of DCT2 sample. (b) Selected twinned region investigated with SAED. The SAED displays austenite matrix (green colour). (c) TEM image depicting twinned austenite structures with large amount of twinning faults (marked with red arrows). (d) Selected region of interest depicting a twinned austenite structure (green colour in SAED, marking only 1 of 3 austenite grain orientations). The centrepiece of the structure holds additionally a single  $\alpha$ -martensite grain (yellow colour in SAED). In the region also  $\epsilon$ -martensite (red colour in SAED) is determined to be present with additional reflections indicating a polycrystalline presence of this phase. The grain boundaries twins with  $\alpha$ -martensite depict a slight contrast variation, which is associated with the formation of carbide-rich zones and carbides caused by the local transformation into martensitic structures (weak diffraction peaks with 0.244 nm spacing marked by orange arrows).

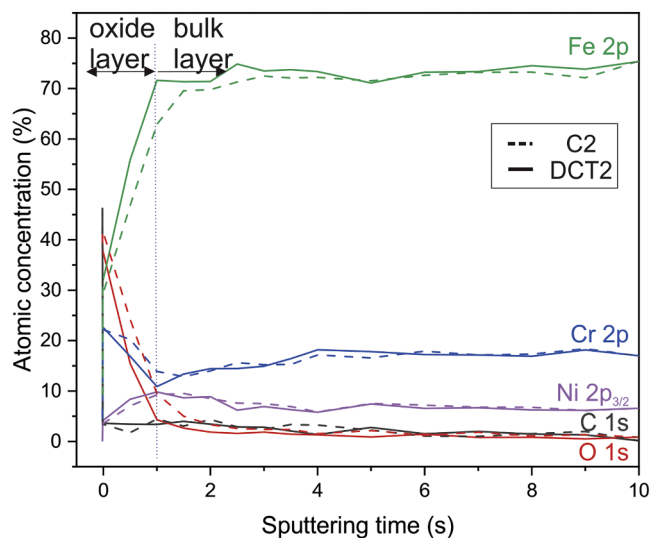


**Fig. 10.** XPS depth profiles of investigated sample C2 (control group-CHT) and DCT2 (tested group-DCT).

preferential formation of  $\text{Fe}_2\text{O}_3$  on the surface of the material compared to C2. However, the Fe-based oxidation system and explanations of Fe is complex [12]. Due to multiple possible peaks and presence of

Fe-satellite peaks at the same binding energy range, multiple peaks can overlap at the same binding energy, posing difficulties in the comparative assessment of the samples. The reason for the complex explanation also in this study is due to the background effect and thin oxide layer on the surface, making the interpretation highly dependent on locality and inhomogeneity of the surface. Overall, in the bulk portion of both samples, the surface specific oxides and carbonates diminish in fraction and the Cr (III) oxide and  $\text{Fe}_2\text{O}_3$  dominate for both samples. The AR-XPS measurements also provide additional confirmation of the presence of  $\text{Cr}_2\text{C}$  and  $\text{Cr}_7\text{C}_3$  carbides [45], as determined already from XRD. The XPS data indicates that the  $\text{M}_7\text{C}_3$  precipitates are more present for the DCT2 sample, which correlates well with the XRD findings. Furthermore, in bulk DCT2 sample C1s spectrum, peak for  $\text{M}_7\text{C}_3$  carbides can also be observed, which additionally confirms precipitation of specific carbides within the matrix. The deconvoluted XPS peak for  $\text{Cr}_2\text{C}$  [45] indicates a generally similar presence of these carbides for both samples, which could be a result of their preferential formation on grain boundaries of the austenite grains. From all the elements, Ni displays no difference between the investigated samples from both surface- and bulk-sensitive AR-XPS spectra.

### 3.5. ToF-SIMS

Samples C2 and DCT2 were also characterized by ToF-SIMS to further evaluate their surface properties and surface-bound chemistry. ToF-SIMS depth profiling was performed with the  $\text{Cs}^+$  ions and

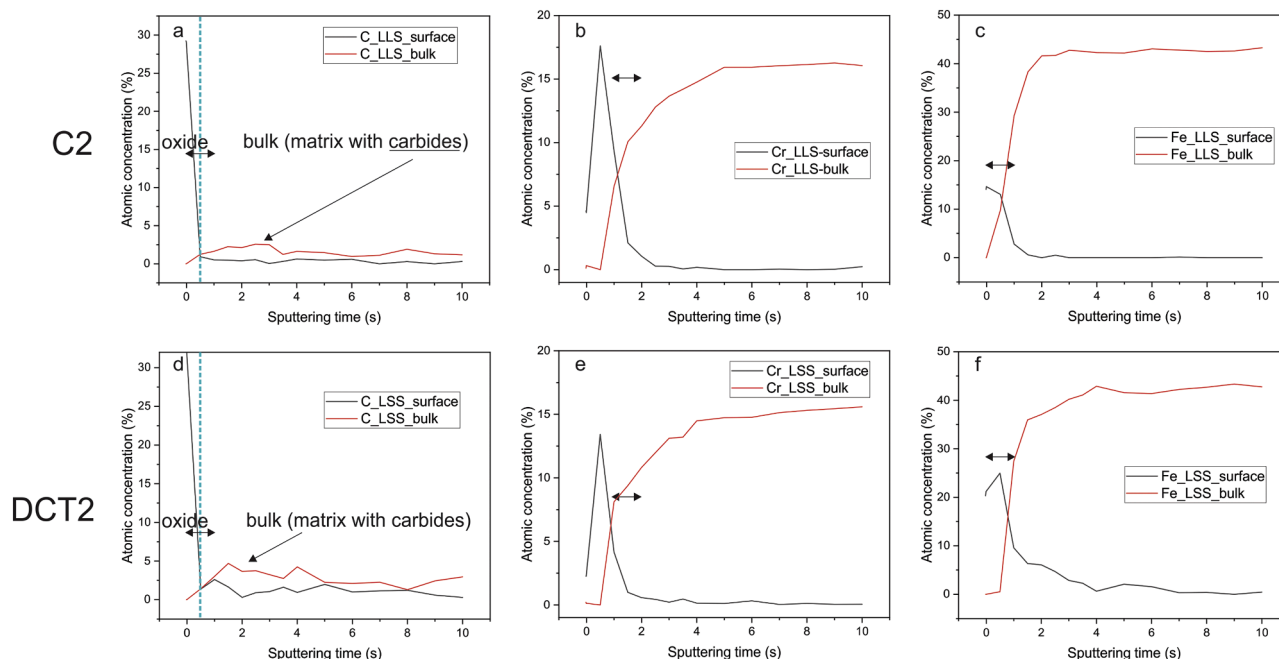


Fig. 11. LLS analysis of the depth profiles of both samples in relation to C (a and d), Cr (b and e) and Fe (c and f).

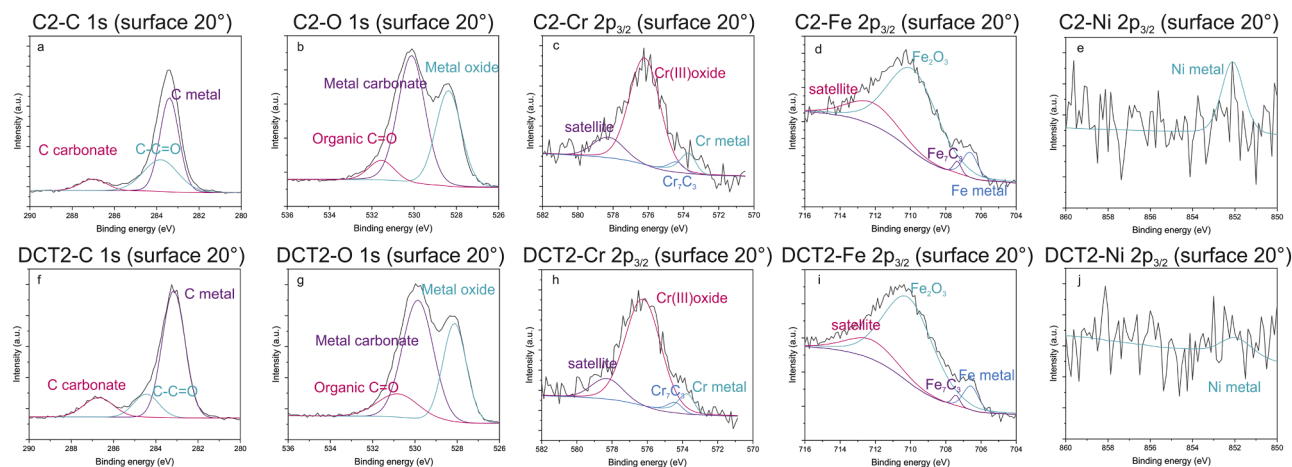


Fig. 12. Angle-resolved XPS spectra for individual elements with low angle of incidence for probing more surface-related chemical information.

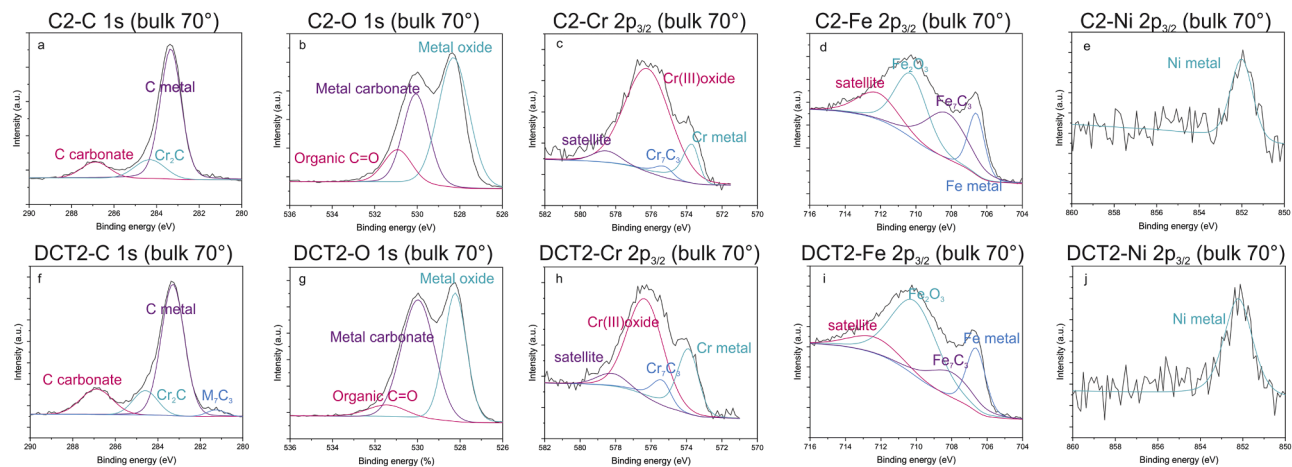


Fig. 13. Angle-resolved XPS spectra for individual elements with high angle of incidence for probing more bulk-related chemical information.

therefore, negative secondary ions were analysed. The results indicate very thin nanolayer of oxide for both samples, confirming results from XPS/AR-XPS (Fig. 14).

The ions  $\text{CN}^-$ ,  $\text{O}_2^-$ ,  $\text{FeH}^-$ ,  $\text{FeO}_2^-$ ,  $\text{CrO}_3^-$  and  $\text{NiH}_2^-$  were the most informative signals extracted from the ToF-SIMS measurements. The thin oxide nanolayer in both samples consists mainly of Fe and Cr, which is confirmed with the  $\text{FeO}_2^-$  and  $\text{CrO}_3^-$  signals. For both samples, C2 and DCT2,  $\text{O}_2^-$  signal indicates the estimated thickness of 2 nm for the oxide layer, which can be further subdivided into Fe-rich ( $\text{FeO}_2^-$ ) oxide and underlying Cr-enriched oxide layer ( $\text{CrO}_3^-$ ). The latter serves as passivation layer, that is common for Cr-rich austenitic stainless steels [46]. With DCT (DCT2) the oxides signals are slightly different compared to the CHT (C2). This can be explained by the exposure to the liquid nitrogen that causes increased oxidation of the layer, due to the nanocracking of the surface and increased oxidation that occurs during warm-up and local condensation effects [19]. This phenomenon also explains the wider and stronger nitrogen enriched layer afterwards (Fig. 14b, signal  $\text{CN}^-$ ), correlating to increased diffusivity of nitrogen into the subsurface of the treated material (Fig. 14). Interestingly, the thickness of the oxide layers, seems to be unmodified by DCT. In retrospect, the nitrogen layer ( $\text{CN}^-$ ) thickens (see 3D reconstructions, Fig. 14a and b), which further supports the increased supply of nitrogen during exposure to liquid nitrogen. Furthermore, deeper portions of the matrix are not modified by DCT, as indicated by the consistent  $\text{FeH}^-$  and  $\text{NiH}_2^-$  signals.

#### 4. Conclusions

The complexity of deep cryogenic treatment and its influence on the microstructure and surface chemistry of austenitic stainless steel AISI 304 L was investigated by the combination of different techniques of LM, SEM/EDS/EBSD, XRD, HRTEM/STEM, XPS/AR-XPS and ToF-SIMS. The presented results deliver valuable input into the DCT dynamic of the DCT heat-treated austenitic stainless steels through the following conclusions:

- Austenitic grains are on average 5 % larger compared to the grains in the control counterparts, which is suggested to be related to the relaxation of internal stresses with DCT. Additionally, twinning is 5-10 % more common in DCT samples in comparison to the control samples.
- The phase analyses (SEM/ESBD, XRD and HRTEM/STEM) confirm that the main phase in all samples is austenite (FCC) with smaller fractions of  $\alpha$ -martensite (BCT),  $\epsilon$ -martensite (HCP),  $\delta$ -ferrite and carbides ( $\text{M}_2\text{C}$  and  $\text{M}_7\text{C}_3$ ), which were enriched mainly with Cr. DCT is shown to increase precipitation of  $\text{M}_7\text{C}_3$  carbides in the expense of  $\text{M}_2\text{C}$  carbides when lower solution-annealing temperature was used. DCT does not influence the preferential orientation direction of any of phases.
- XPS-LLS confirms that the structure of the oxide layer is different between CHT and DCT samples. CHT sample has a higher fraction of Cr and a lower Fe fraction in the oxide layer compared to DCT sample.

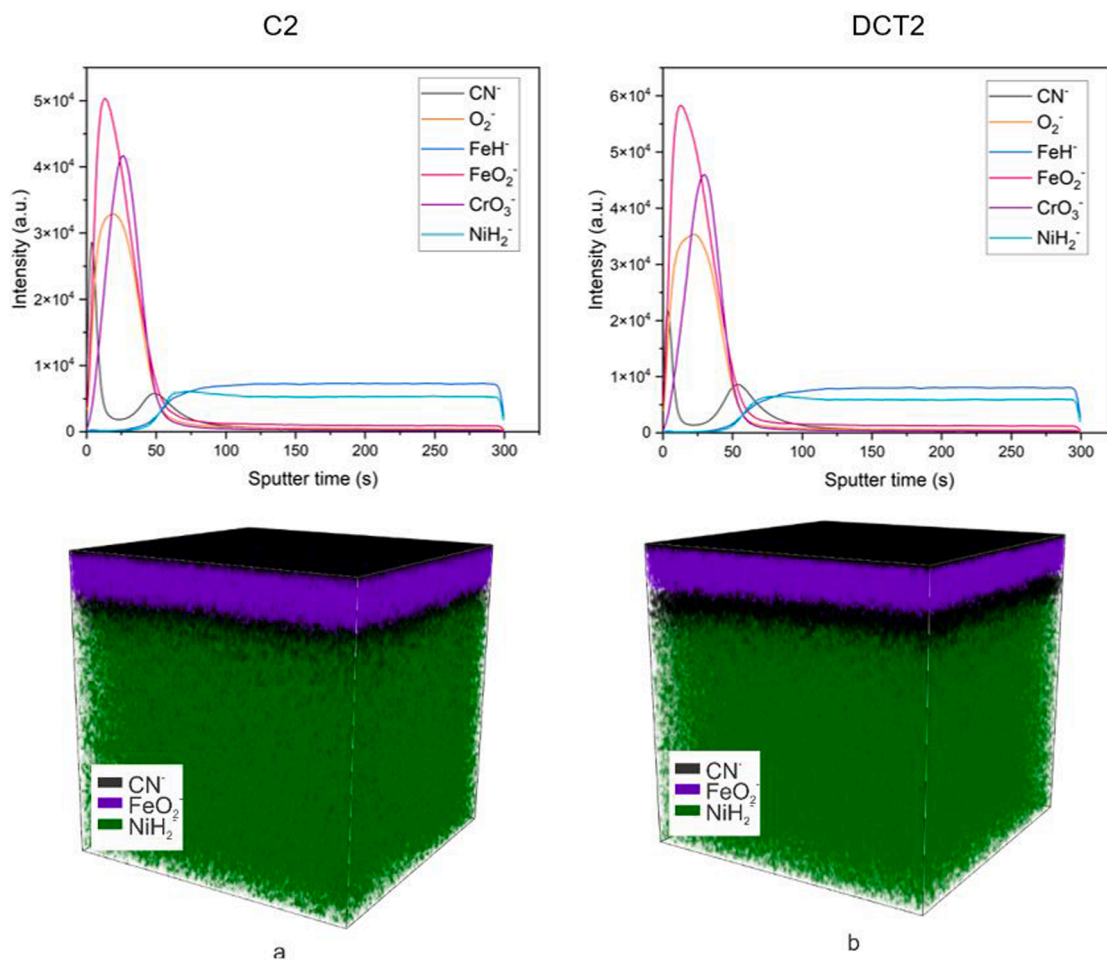


**Fig. 14.** Represents the results from ToF-SIMS depth profiling with the most relevant ions and corresponding ToF-SIMS 3D plots with selected representative ions for each layer of the samples of area  $100 \times 100 \mu\text{m}$ . a) ToF-SIMS profile and ToF-SIMS 3D plots of control sample C2 and b) ToF-SIMS profile and ToF-SIMS 3D plots of tested sample with DCT-DCT2.



- AR-XPS results shows that DCT sample has higher oxygenation of the surface as sample CHT: The AR-XPS measurements also provide additional confirmation of the presence of Cr<sub>2</sub>C and Cr<sub>7</sub>C<sub>3</sub> carbides.
- ToF-SIMS confirms that DCT modifies nitrogen diffusivity and activity within the matrix.
- DCT influences both microstructure development as well as surface oxidation dynamics.

## Funding

This work was supported by Slovenian Research Agency (ARRS), Ljubljana, Slovenia [Nos. P2-0050 & J2-9211].

## Data availability

The raw/processed data required to reproduce these findings cannot be shared at this time as the data also forms part of an ongoing study.

## CRediT authorship contribution statement

**Patricia Jovičević-Klug:** Conceptualization, Methodology, Investigation, Resources, Writing – original draft, Writing – review & editing, Visualization. **Nataša Lipovšek:** Methodology, Investigation, Resources, Writing – original draft, Writing – review & editing. **Matic Jovičević-Klug:** Conceptualization, Methodology, Investigation, Writing – original draft, Writing – review & editing. **Maruša Mrak:** Methodology, Resources, Writing – original draft, Writing – review & editing. **Jernej Ekar:** Methodology, Resources, Writing – original draft, Writing – review & editing. **Bojan Ambrožič:** Methodology, Resources, Writing – original draft, Writing – review & editing. **Goran Dražič:** Methodology, Resources, Writing – review & editing. **Janez Kovač:** Methodology, Resources, Writing – review & editing. **Bojan Podgornik:** Supervision, Resources, Writing – review & editing.

## Declaration of Competing Interest

The authors declare no competing interests.

## Data Availability

Data will be made available on request.

## Acknowledgment

The authors would like to thank Dr. Barbara Šetina Batič for the help with SEM measurements and Tatjana Filipič for the help with XPS measurements.

## Supplementary materials

Supplementary material associated with this article can be found, in the online version, at doi:10.1016/j.surf.2022.102456.

## References

- [1] F. Cattant, D. Crusset, D. Féron, Corrosion issues in nuclear industry today, *Mater. Today* 11 (2008) 32–37, [https://doi.org/10.1016/S1369-7021\(08\)70205-0](https://doi.org/10.1016/S1369-7021(08)70205-0).
- [2] C. Okonkwo Paul, A. Shakoar, A.M.A. Mohamed, Environmental factors affecting corrosion of pipeline steel: a review, *Int. J. Mech. Prod. Eng. Res. Dev.* 5 (2015) 57–70, <https://doi.org/10.1021/bk-1986-0318.ch009> (JMPERD).
- [3] H. Parangusan, J. Bhadra, N. Al-Thani, A review of passivity breakdown on metal surfaces: influence of chloride- and sulfide-ion concentrations, temperature, and pH, *Emerg. Mater.* 4 (2021) 1187–1203, <https://doi.org/10.1007/S42247-021-00194-6> (FIGURES/18).
- [4] S.M. Perren, P. Regazzoni, A.A. Fernandez, How to choose between the implant materials steel and titanium in orthopedic trauma surgery: Part 2 - biological aspects, *Acta Chir. Orthop. Traumatol. Cech.* 84 (2017) 85–90.
- [5] KUKA, KUKA robotics to provide stainless steel robot for food application, *Ind. Robot Int. J.* 34 (2007), <https://doi.org/10.1108/IR.2007.04934DAD.002>.
- [6] P. Snelgrove, Stainless steel automotive and transport developments, *Worldstainless* (2002) 1–5. <http://www.worldstainless.org/library/> (accessed January 18, 2022).
- [7] M. Gasdia-Cochrane, New applications for stainless steel in mining, (2018), 1–2. <https://www.thermofisher.com/blog/mining/new-applications-for-stainless-steel-in-mining/>. (accessed January 18, 2022).
- [8] A. Zaffora, F. di Franco, M. Santamaria, Corrosion of stainless steel in food and pharmaceutical industry, *Curr. Opin. Electrochem.* 29 (2021), 100760, <https://doi.org/10.1016/J.COEELEC.2021.100760>.
- [9] L. Gardner, Stability and design of stainless steel structures – review and outlook, *Thin Walled Struct.* 141 (2019) 208–216, <https://doi.org/10.1016/J.TWS.2019.04.019>.
- [10] C.O.A. Olsson, D. Landolt, Passive films on stainless steels - chemistry, structure and growth, *Electrochim. Acta* 48 (2003) 1093–1104, [https://doi.org/10.1016/S0013-4686\(02\)00841-1](https://doi.org/10.1016/S0013-4686(02)00841-1).
- [11] M.F. McGuire, *Stainless Steels for Design Engineers*, ASM International, Almere, Netherlands, 2008.
- [12] S. Tardio, M.L. Abel, R.H. Carr, J.H. Castle, J.F. Watts, Comparative study of the native oxide on 316L stainless steel by XPS and ToF-SIMS, *J. Vac. Sci. Technol. A Vac. Surf. Films* 33 (2015) 122, <https://doi.org/10.1116/1.4927319>.
- [13] B. Lynch, S. Neupane, F. Wiame, A. Seyeux, V. Maurice, P. Marcus, An XPS and ToF-SIMS study of the passive film formed on a model FeCrNiMo stainless steel surface in aqueous media after thermal pre-oxidation at ultra-low oxygen pressure, *Appl. Surf. Sci.* 554 (2021), 149435, <https://doi.org/10.1016/J.APSUSC.2021.149435>.
- [14] L.T. Popoola, A.S. Grema, G.K. Latinwo, B. Gutti, A.S. Balogun, Corrosion problems during oil and gas production and its mitigation, *Int. J.* 4 (2013) 1–15, <https://doi.org/10.1186/2228-5547-4-35/FIGURES/20>.
- [15] N. Eliaz, Corrosion of metallic biomaterials: a review, *materials* 12 (2019) 407, <https://doi.org/10.3390/MA12030407>.
- [16] J.A. Puentes Parodi, Adhesion of polyurethane-steel hybrids and influence of annealing on its durability and lifetime, 2018.
- [17] S. Kasala, M. Vidyavathy, M.S. Vidyavathy, Advanced ceramic coatings on stainless steel: a review of research, methods, Mater. Appl. Oppor. (2016) n.d. <https://www.researchgate.net/publication/305473617>.
- [18] J. Voglar, Ž. Novak, P. Jovičević-Klug, B. Podgornik, T. Kosec, Effect of deep cryogenic treatment on corrosion properties of various high-speed steels, *Metals* 11 (2020) 14, <https://doi.org/10.3390/met11010014>.
- [19] M. Jovičević-Klug, P. Jovičević-Klug, T. Kranjec, B. Podgornik, Cross-effect of surface finishing and deep cryogenic treatment on corrosion resistance of AISI M35 steel, *J. Mater. Res. Technol.* 14 (2021) 2365–2381, <https://doi.org/10.1016/j.jmrt.2021.07.134>.
- [20] S. Ramesh, B. Bhuvaneshwari, G.S. Palani, D. Mohan Lal, K. Mondal, R.K. Gupta, Enhancing the corrosion resistance performance of structural steel via a novel deep cryogenic treatment process, *Vacuum* 159 (2019) 468–475, <https://doi.org/10.1016/j.vacuum.2018.10.080>.
- [21] S. Ramesh, B. Bhuvaneshwari, G.S. Palani, D.M. Lal, N.R. Iyer, Effects on corrosion resistance of rebar subjected to deep cryogenic treatment, *J. Mech. Sci. Technol.* 31 (2017) 123–132, <https://doi.org/10.1007/s12206-016-1211-5>.
- [22] W. Wang, V. Srinivasan, S. Siva, B. Albert, M. Lal, A. Alfantazi, Corrosion behavior of deep cryogenically treated AISI 420 and AISI 52100 steel, *Corrosion* 70 (2014) 708–720, <https://doi.org/10.5006/1150>.
- [23] X. Gong, Z. Wu, F. Zhao, Effect of deep cryogenic treatment on the microstructure and the corrosion resistance of AZ61 magnesium alloy welded joint, *Metals* 7 (2017) 179, <https://doi.org/10.3390/met7050179>.
- [24] P. Jovičević-Klug, T. Kranjec, M. Jovičević-Klug, T. Kosec, B. Podgornik, Influence of the deep cryogenic treatment on AISI 52100 and AISI D3 Steel's corrosion resistance, *Materials* 14 (2021) 6357, <https://doi.org/10.3390/MA14216357>, 2021Page146357.
- [25] D. Senthilkumar, G.E. Totten, R. Colas, *Cryogenic treatment: shallow and deep*. Encyclopedia of Iron, Steel, and Their Alloys, Taylor and Francis, NY, USA, New York, NY, 2016, pp. 995–1007, <https://doi.org/10.1081/E-EISA-120052805>.
- [26] P. Baldissera, C. Delprete, Deep cryogenic treatment: a bibliographic review, *Open Mech. Eng. J.* 2 (2008) 1–11, <https://doi.org/10.2174/1874155X00802010001>.
- [27] P. Jovičević-Klug, B. Podgornik, Review on the effect of deep cryogenic, *Metals* 10 (2020) 434–444, <https://doi.org/10.3390/met10040434>.
- [28] R.F. Barron, Cryogenic treatment of metals to improve wear resistance, *Cryogenics* 22 (1982) 409–413, [https://doi.org/10.1016/0011-2275\(82\)90085-6](https://doi.org/10.1016/0011-2275(82)90085-6).
- [29] P. Baldissera, C. Delprete, Deep cryogenic treatment of AISI 302 stainless steel: Part II - fatigue and corrosion, *Mater. Des.* 31 (2010) 4731–4737, <https://doi.org/10.1016/j.matdes.2010.05.015>.
- [30] P. Baldissera, C. Delprete, Deep cryogenic treatment of AISI 302 stainless steel: Part II - fatigue and corrosion, *Mater. Des.* 31 (2010) 4731–4737.
- [31] P. Baldissera, S. Cavalleri, P. Marcelloni, F. Tordini, Study of the effect of DCT and PVD treatments on the fatigue behaviour of AISI 302 stainless steel, *Key Eng. Mater.* 417–418 (2010) 49–52, <https://doi.org/10.4028/www.scientific.net/KEM.417-418.49>.
- [32] J.D. Darwin, D. Mohan Lal, G. Nagarajan, Optimization of cryogenic treatment to maximize the wear resistance of 18% Cr martensitic stainless steel by Taguchi method, *J. Mater. Process. Technol.* 195 (2008) 241–247, <https://doi.org/10.1016/j.jmatprotec.2007.05.005>.
- [33] P. Jovičević-Klug, M. Jovičević-Klug, T. Sever, D. Feizpour, B. Podgornik, Impact of steel type, composition and heat treatment parameters on effectiveness of deep

- cryogenic treatment, *J. Mater. Res. Technol.* 14 (2021) 1007–1020, [10.1016/j.jmrt.2021.07.022](https://doi.org/10.1016/j.jmrt.2021.07.022).
- [34] H.M. Rietveld, A profile refinement method for nuclear and magnetic structures, *J. Appl. Crystallogr.* 2 (1969) 65–71, <https://doi.org/10.1107/s0021889869006558>.
- [35] H. Toraya, A new method for quantitative phase analysis using X-ray powder diffraction: direct derivation of weight fractions from observed integrated intensities and chemical compositions of individual phases, *J. Appl. Crystallogr.* 49 (2016) 1508–1516, <https://doi.org/10.1107/S1600576716010451>.
- [36] J. Ekar, P. Panjan, S. Drev, J. Kovač, ToF-SIMS depth profiling of metal, metal oxide, and alloy multilayers in atmospheres of H<sub>2</sub>, C<sub>2</sub>H<sub>2</sub>, CO, and O<sub>2</sub>, *J. Am. Soc. Mass. Spectrom.* 33 (2022) 31–44, <https://doi.org/10.1021/jasms.1c00218>.
- [37] B. He, On the factors governing austenite stability: intrinsic versus extrinsic, *Materials* 13 (2020) 1–31, <https://doi.org/10.3390/MA13153440>.
- [38] E. Schaffler, K. Simon, S. Bernstorff, P. Hanák, G. Tichy, T. Ungár, M.J. Zehetbauer, A second-order phase-transformation of the dislocation structure during plastic deformation determined by *in situ* synchrotron X-ray diffraction, *Acta Mater.* 53 (2005) 315–322, <https://doi.org/10.1016/J.ACTAMAT.2004.09.025>.
- [39] B. Li, C. Li, Y. Wang, X. Jin, Effect of cryogenic treatment on microstructure and wear resistance of carburized 20CrNi2MoV steel, *Metals* 8 (2018), <https://doi.org/10.3390/met8100808>.
- [40] K. Gu, H. Zhang, B. Zhao, J. Wang, Y. Zhou, Z. Li, Effect of cryogenic treatment and aging treatment on the tensile properties and microstructure of Ti-6Al-4V alloy, *Mater. Sci. Eng. A* 584 (2013) 170–176, <https://doi.org/10.1016/j.msea.2013.07.021>.
- [41] B. Che, L. Lu, J. Zhang, J. Zhang, M. Ma, L. Wang, F. Qi, Effects of cryogenic treatment on microstructure and mechanical properties of AZ31 magnesium alloy rolled at different paths 832 (2022) 142475, <https://doi.org/10.1016/j.msea.2021.142475>.
- [42] Y.F. Shen, X.X. Li, X. Sun, Y.D. Wang, L. Zuo, Twinning and martensite in a 304 austenitic stainless steel, *Mater. Sci. Eng. A Struct. Mater.* 552 (2012) 514–522, <https://doi.org/10.1016/J.MSEA.2012.05.080>.
- [43] B. Kim, J. Sietsma, M.J. Santofimia, The role of silicon in carbon partitioning processes in martensite/austenite microstructures, *Mater. Des.* 127 (2017) 336–345, <https://doi.org/10.1016/J.MATDES.2017.04.080>.
- [44] R.E. Smallman, A.H.W. Ngan, Surfaces, grain boundaries and interfaces. Modern Physical Metallurgy, Butterworth-Heinemann, Oxford, UK, 2014, pp. 415–442, <https://doi.org/10.1016/B978-0-08-098204-5.00010-9>.
- [45] C. Boonruang, W. Sanumang, Effect of nano-grain carbide formation on electrochemical behavior of 316L stainless steel, *Sci. Rep.* 11 (1) (2021) 1–11, <https://doi.org/10.1038/s41598-021-91958-x>, 202111.
- [46] F. Riffard, H. Buscail, E. Caudron, R. Cuffe, F. Rabaste, C. Issartel, *In situ* and glancing angle X-ray diffraction of the structure change during and after the high temperature oxidation at 1000°C in air of an yttrium-implanted 304 steel, *J. Phys. IV* 12 (2002) 265–272, <https://doi.org/10.1051/JP4:20020235> (Proceedings).